

Clock Dynamics Analysis in IMM Filter for Carrier Phase Estimation Through Interference

Wengxiang Zhao, *Illinois Institute of Technology*
Samer Khanafseh, *Illinois Institute of Technology*
Boris Pervan, *Illinois Institute of Technology*

ABSTRACT

In this paper, we develop a dynamic model of receiver clock phase noise to enable Interactive Multiple Model (IMM) filters to maintain GPS carrier phase lock through broadband interference. Further, we extend the model to include the effects of vibration on clock phase noise. A covariance analysis is conducted to check our filter performance. Experimental validation results under normal and interference cases are provided. The clock dynamic model parameter sensitivity is analyzed to give some insight on the potential use of different types of clocks and to improve the robustness of the IMM filter.

I. INTRODUCTION

Along with the growing demand for GPS services, intentional and unintentional jamming and spoofing are happening more frequently than in the past. In this paper, we take the Ground Based Augmentation System (GBAS) reference station receiver as an example [1] to evaluate the performance of the carrier phase estimation under wide band radio frequency interference (RFI). The goal of this research is to develop a robust GPS receiver to estimate the carrier phase and preserve the continuity throughout the interference event.

In prior work, we introduced an Interacting Multiple Model (IMM) filter to take over the function of the traditional Phase Lock Loop (PLL) to do the carrier phase estimation. In prior work [2], a simple simulation-based validation was done for static phase, and the effect of navigation data bit knowledge on the estimation result was discussed. In [3], we validated the IMM filter with experimental data under the no-interference case. The IMM filter was able to produce the same carrier phase estimate as the PLL in a normal signal strength scenario. In [4], we extended the coherent averaging time to 20 ms for both PLL and IMM and proved the advantages of the IMM filter over PLL in the interference case.

In this paper, we use a new method to derive the clock dynamic model, which extends the clock phase noise power spectral density (PSD) to the full frequency range relevant to phase tracking. Furthermore, the clock model is extended to the vibration case for future applications in aircraft or ground vehicles. We perform a sensitivity covariance analysis and quantify the IMM filter convergence performance. We show that good IMM filter performance does not require an atomic clock.

In Section II, the IMM algorithm is explained and the component Kalman filters are set up. Section III derives a dynamic model for clock phase dynamics. Section IV performs the covariance analysis. Section V discusses the simulation result for the IMM filter with a static phase. Section VI describes the experimental scenario and setup. Section VII provides an experimental validation of the IMM filter under normal conditions (no interference). Section VIII shows the IMM filter experimental results in the presence of interference. Section IX investigates the sensitivity of the carrier phase estimation result on the clock dynamic model.

II. KALMAN FILTER AND IMM ALGORITHM

While typical PLLs have a fixed structure with predefined loop filters, Kalman filters have internal adaptability to rely more heavily on either measurements or phase dynamics depending on the noise levels. Extended coherent averaging times are needed to track through interference. If there is no external information about the navigation data bits, the maximum coherent integration time is 20 ms, which is the duration of one navigation data bit. However, if possible, longer coherent integration

times can help immensely to average out noise, resulting in much cleaner I and Q measurements (Inphase and Quadrature, respectively).

In SDR architectures (software-defined radios), carrier phase and code phase tracking loops start with the carrier frequency obtained from the acquisition process. Mixing the raw received signal with local sine and cosine waves at the acquired carrier frequency will produce I and Q measurements. Moving forward, the carrier tracking loop will update the local carrier frequency using I and Q measurements averaged over each subsequent coherent integration window. Figure 1 shows the carrier phase tracking architecture in an SDR.

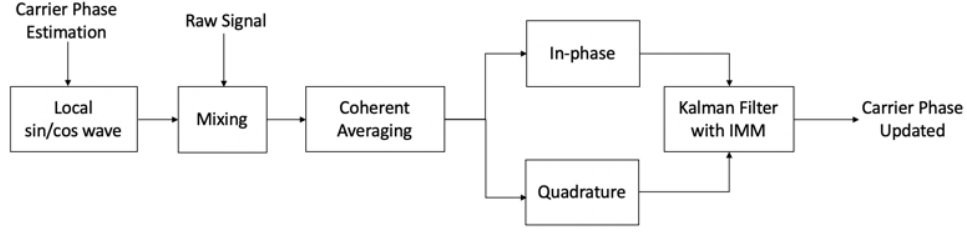


Fig. 1. Carrier phase tracking in SDR

Both the carrier phase and code phase tracking loops rely on the determination of carrier frequency, which means the quality of I and Q measurements is extremely important. The interference event contributes additive white Gaussian noise (AWGN) directly into I and Q measurements. For typical PLL operation, using a simple phase discriminator, these noisy measurements can easily cause phase errors exceeding the pull-in limit of phase discriminator, usually leading to cycle slips and eventual loss of lock.

The shortcomings of a traditional PLL can be overcome using a Kalman filter to estimate phase directly. The goal of any carrier phase tracking loop is to produce the best phase estimate under noisy conditions. The Kalman filter does precisely this given that the noise is white, which is the case in wideband interference. In our interference scenario, the receiver is running normally when hit by an RFI event, so the Kalman filter estimate error is small at the start.

A. Dynamic model

The clock phase noise can be modeled using a second order system. The details of the model will be discussed in Section III.

$$\begin{bmatrix} \dot{\phi}_{clk} \\ \phi_{clk} \end{bmatrix}_{k+1} = \Phi \begin{bmatrix} \dot{\phi}_{clk} \\ \phi_{clk} \end{bmatrix}_k + w_k \quad (1)$$

where k is a time index defining the current coherent average interval.

Over one coherent averaging interval, the total phase change is $\Delta\phi_{tot} = \Delta\phi_{sm} + \Delta\phi_{clk}$, where $\Delta\phi_{sm}$ is the phase change due to satellite movement relative to the receiver. For our current development, we assume a static receiver, e.g., a GBAS reference receiver, so that $\Delta\phi_{sm}$ is the result of satellite motion only, which is known using the broadcast ephemeris. In future work for moving users, the relative motion between satellite and receiver can be accommodated using inertial sensors.

B. Measurement model

The measurement model can be written as

$$I_k = d_k A_k \cos(\Delta\phi_{tot,k}) + v_{i,k} \quad (2)$$

$$Q_k = d_k A_k \sin(\Delta\phi_{tot,k}) + v_{q,k} \quad (3)$$

where d is the navigation data bit, A is the signal amplitude, and v_i and v_q are i.i.d. $\sim N(0, V)$, where $V = I\sigma_v^2$ and is related to the carrier-to-noise ratio as follows:

$$C/N_0 = 10^{\frac{C/N_0(\text{dBHz})}{10}} \quad (4)$$

$$\sigma_v = \frac{1}{\sqrt{0.04 C/N_0}} \quad (5)$$

C. IMM algorithm

The IMM is a multiple hypothesis estimation algorithm. It assumes a system obeys one of a finite number of models at a time [5]. It is composed of the five steps shown in Figure 2. Starting with prior probabilities of each model being correct, parallel Kalman updates are executed for each, and the mode likelihood functions are evaluated based on the measurements. Then post measurement mode probabilities are determined, and the results from all of the modes are weighted and combined to produce the output state vector estimate and its error covariance matrix.

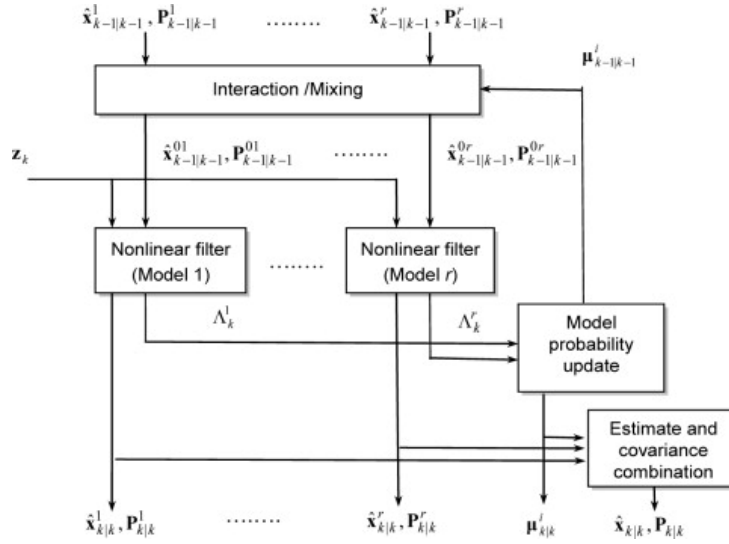


Fig. 2. Standard IMM algorithm

In our IMM application, as shown in Figure 3, two modes run in parallel, corresponding to the two navigation data bits values, 1 and -1 . The mode (bit) transition probabilities are 50% and 50%, which means the data bits are sequentially independent of each other. However, the data bits in reality are not totally random. The knowledge of some navigation data bits can also be utilized by the IMM, as we have shown in our prior work [2]. We assume no such knowledge here.

III. CLOCK DYNAMIC MODEL

In traditional PLL, carrier phase tracking is realized by continuously compensating phase error between incoming signal and local replica signal using the phase discriminator output results. I and Q samples are the only information sent into the phase discriminator. When the quality of current I and Q samples are influenced by the interference event, the discriminator cannot output the accurate compensation value for the carrier phase. The mistakes in phase compensation will accumulate over time leading to cycle slips, and eventually, loss of lock. This is the primary reason why receiver PLL cannot maintain tracking under strong interference events.

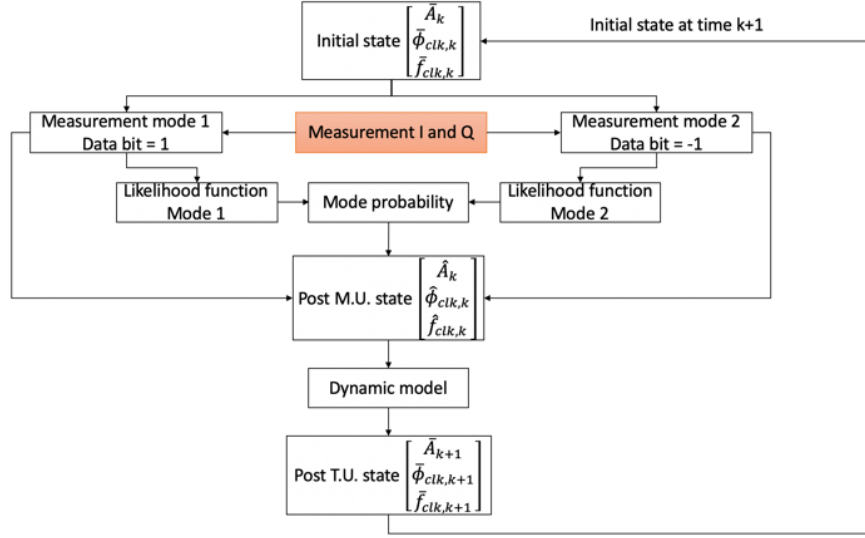


Fig. 3. IMM algorithm in our application

In order to counter the potential quality drop of the measurement I and Q samples, we could provide a relatively stable dynamic model to the IMM filter because the IMM Kalman filter has the inherent ability to trust the dynamic model more when the measurement noise is huge. A good choice for this would be the clock phase dynamic model for two reasons. First, our goal is trying to estimate the carrier phase which contains Doppler, clock phase, ionosphere, troposphere, and thermal noise. We can exclude the Doppler portion if we have access to the navigation data message, which we do from the previously broadcast ephemeris. The main component remaining is the clock phase. Second, there are many prior research efforts on different GPS clock parameters and modeling that we can use.

Also, if we had a clock phase dynamic model, the IMM filter would not have to do the estimation from scratch at every time epoch without utilizing any past information on carrier phase. At each time epoch, the IMM filter will have the old carrier phase information from the propagation of the dynamic model and the new measurement I and Q samples to produce the next carrier phase estimate. All this gives us a strong motivation to derive the clock dynamic model and apply it in our IMM filter.

A. Rubidium clock

We use separate Rubidium atomic oscillators, both SpectraTime, Low Cost & Profile Frequency Rubidium Standards (LPFRS), in our experimental work for both the receiver and GPS signal simulator. The LPFRS Rubidium clock has better long-term stability and less phase noise than TCXO and many OCXO clocks which allows the PLL to tighten a narrower noise bandwidth and reach its best performance under interference events. We are trying to make a fair comparison between our IMM filter and a traditional PLL. We want the IMM filter to compete with the PLL peak performance, hence our choice of the Rubidium clock. However, in Section IX, we show that the IMM filter can achieve good performance even with the TCXO clocks.

1) Full Frequency Range Phase Noise Power Spectral Density (PSD): The clock product specifications only provide the phase noise PSD data at a few discrete points between 1 and 10000 Hz. It did not cover the phase noise PSD in lower frequency ranges (below 1 Hz). We do care about the lower frequencies for the vibration case model derivation.

The random fluctuation in phase, corresponding to jitter in the time domain (Allan variance), is described by the clock's phase noise PSD, which is modeled as:

$$S_{\phi}(f) = h_2 f^0 + h_1 f^{-1} + h_0 f^{-2} + h_{-1} f^{-3} + h_{-2} f^{-4} \quad (6)$$

To determine a set of h coefficients, we started with the clock's the Allan variance data in the specifications. The relationship between Allan variance ($\sigma_y^2(\tau)$) and phase noise PSD ($S_{\phi}(f)$) is shown in Figure 4 from [6].

Description of noise process	$S_y(f) =$	$S_\phi(f) =$	$\sigma_y^2(\tau) =$
Random walk FM	$h_{-2}f^{-2}$	$h_{-2}v^2f^{-4}$	$Ah_{-2}\tau^1$
Flicker FM	$h_{-1}f^{-1}$	$h_{-1}v^2f^{-3}$	$Bh_{-1}\tau^0$
White FM	h_0f^0	$h_0v^2f^{-2}$	$Ch_0\tau^{-1}$
Flicker PM	h_1f^1	$h_1v^2f^{-1}$	$Dh_1\tau^{-2}$
White PM	h_2f^2	$h_2v^2f^0$	$Eh_2\tau^{-2}$

$$A = \frac{2\pi^2}{3} \quad B = 2 \ln 2 \quad C = 1/2$$

$$D = \frac{1.038 + 3 \ln(2\pi f_h \tau)}{4\pi^2} \quad E = \frac{3f_h}{4\pi^2}$$

Fig. 4. Allan variance calculation [6]

We bounded the original Allan variance plot from the clock specifications with $h_2 = 0, h_1 = 0, h_0 = 5 \times 10^{-25}, h_{-1} = 0, h_{-2} = 1 \times 10^{-30}$, which cover a wide frequency range, as shown in the noise PSD plot bound as the red curves in Figure 5.

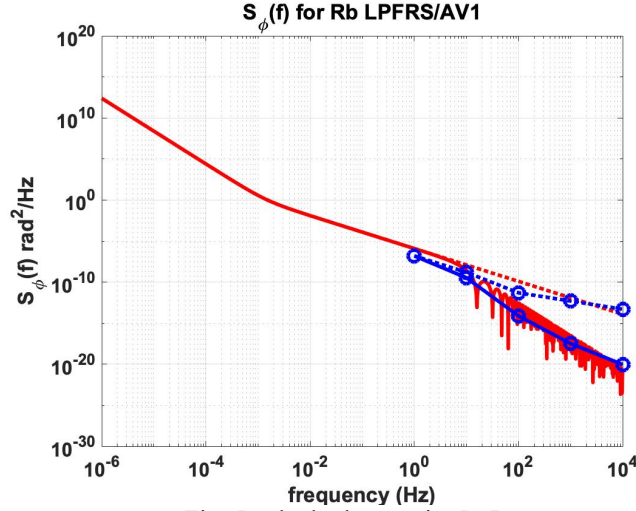


Fig. 5. Clock phase noise PSD

In Figure 5, the blue circles are the only five data points we have from the phase noise PSD specifications (1, 10, 100, 1000, 10000 Hz). Solid lines or circles represent adding coherent integration operation and the dashed lines or circles mean without coherent integration.

The red solid or dashed lines perfectly bound the blue data points because we derive the h coefficients from a bound line in the Allan variance plot. In this way, we successfully extend our Rubidium clock phase noise PSD plot to full frequency range.

2) State Space Realization: According to Section II-A, we write the clock dynamics in discrete state space form with T_s as the coherent averaging time.

$$\begin{bmatrix} \phi \\ \dot{\phi} \end{bmatrix}_{k+1} = \begin{bmatrix} 1 & T_s \\ 0 & 1 \end{bmatrix} \begin{bmatrix} \phi \\ \dot{\phi} \end{bmatrix}_k + w_k \quad (7)$$

where the covariance for the process noise matrix w_k can be written [7] as

$$W = \begin{bmatrix} S_f T_s + \frac{S_g T_s^3}{3} & \frac{S_g T_s^2}{2} \\ \frac{S_g T_s^2}{2} & \frac{S_f}{\Delta t} + \frac{4S_g \Delta t}{3} \end{bmatrix} \quad (8)$$

and $S_g = 2\pi^2 h_{-2}$, $S_f = \frac{h_0}{2}$.

3) Clock Dynamic Model Simulation: A clock phase dynamics simulation was done with $T_s = 1$ ms by simply propagating the dynamic model. Figure 6 shows the phase and frequency error over time.

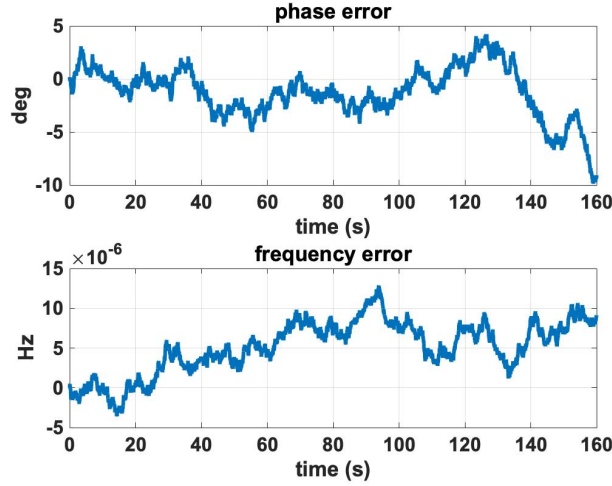


Fig. 6. Clock dynamics simulation

From Figure 6, we get a rough idea that clock frequency drift is at about a 10^{-6} Hz level in 160 seconds without any measurement input. This result could be used for comparison with the actual experimental test results.

B. Vibration model

Modern GPS receiver clocks, including quartz crystal oscillator and atomic clocks, vibrate at a precise frequency when a voltage is applied to them. When a receiver clock's platform is in a vibration environment, like aircraft vibration due to gusts or ground vehicles accelerating up and down due to bad road conditions, the frequency and time counting generated by the clocks may no longer be accurate. Considering that this research will apply to aircraft in the future, a clock model for the vibration case must be derived. This clock model should bound the phase and frequency noise PSD for the vibration case PSD in the worst case. Since we already have the method from h coefficients to the dynamic model, we only need to find a new set of h coefficients that generate the PSD bound for the vibration case.

In the presence of mechanical vibration, the single-sideband oscillator phase noise spectral density $G_\phi(f)$ in rad^2/Hz is going to increase by the term [8]:

$$G_{\phi,vib}(f) = (k_g N f_0)^2 \frac{G_g(f)}{f^2} \quad (9)$$

where k_g is the oscillator's g -sensitivity in parts/ g and N is the acceleration in g 's. Here we use the upper bound provided by the receiver specification for $k_g N$, 2×10^{-10} . f_0 is the oscillator frequency (L1 in our case). $G_g(f)$ is the single-sided vibration spectral density in g^2/Hz . Here we are using a typical $G_g(f)$ vibration spectral density curve for an instrument panel installation on a turbojet aircraft as presented in [9].

By inflating the h coefficients to $h_0 = 2 \times 10^{-21}$, $h_{-2} = 1 \times 10^{-30}$, this set of h coefficients give the PSD bounds for the vibration case phase and frequency PSD. The results are shown in Figure 7 for the phase noise PSD bound and Figure 8 for the frequency PSD bound.

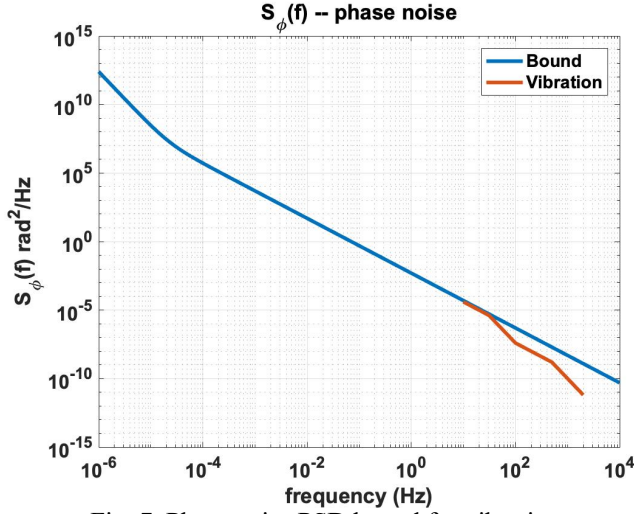


Fig. 7. Phase noise PSD bound for vibration

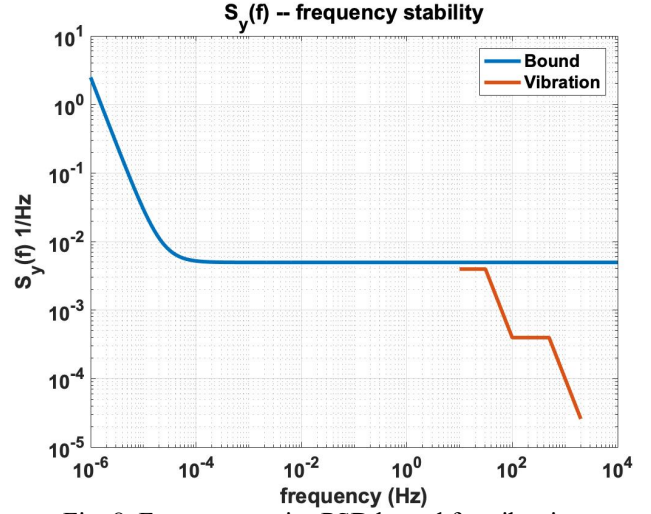


Fig. 8. Frequency noise PSD bound for vibration

In both figures, the red line is the actual PSD curve in the vibration case and the blue line is the bounding curve obtained using $h_0 = 2 \times 10^{-21}$, $h_{-2} = 1 \times 10^{-30}$. The Rubidium clock dynamic model for the vibration case can be derived through the same process as in Equation (8).

IV. COVARIANCE ANALYSIS

Since we already have the measurement noise matrix V and process noise matrix W , it is worth doing a covariance analysis before dealing with actual measurements. The covariance analysis result tells us how quickly the error converges, and which of the two noise matrices is dominant. The initial state covariance is estimated from PLL tracking results. A 1 ms coherent averaging time and $C/N_0 = 51$ dB/Hz is used in this analysis.

The result for the frequency state is shown in Figure 9. The state covariance converges quickly (within 1 second). The Figure 9 inset shows the relative interaction between measurement noise and process noise. The blue circles represent the covariance before measurement update (\bar{P}) and the red crosses represents the covariances after measurement update (\hat{P}). Note that the line from previous red cross to the next blue circle is almost flat. This indicates that the dynamic propagation is not pumping much noise into the IMM filter and so the measurement update is able to bring the covariance down. This meets our expectations given the high-quality Rubidium clock.

This also aligned with our design idea that we want a stable clock dynamic model to provide extra robustness for the IMM filter. With this extra robustness, under an interference event, when the measurement quality is bad and measurement noise is huge, the IMM filter still has a dynamic model to rely on to make the correct carrier phase estimation.

V. SIMULATION

In prior work [2] we did a Monte Carlo simulation with static phase at 135° , with no clock dynamics involved, $C/N_0 = 15$ dB/Hz, 20 ms coherent averaging time, and 100 sequential measurements generated. The result is shown as Figure 10.

Most of the phase estimates are located near 135° . But there is another small peak at -45° caused by wrong data bit estimation by the IMM filter. In [2] we showed that with partial knowledge of navigation data bits, the incorrect peak at -45° can be greatly reduced. The dispersion is a bimodal Gaussian distribution. The sample standard deviation computed using the data points near the peak at 135° is 12° .

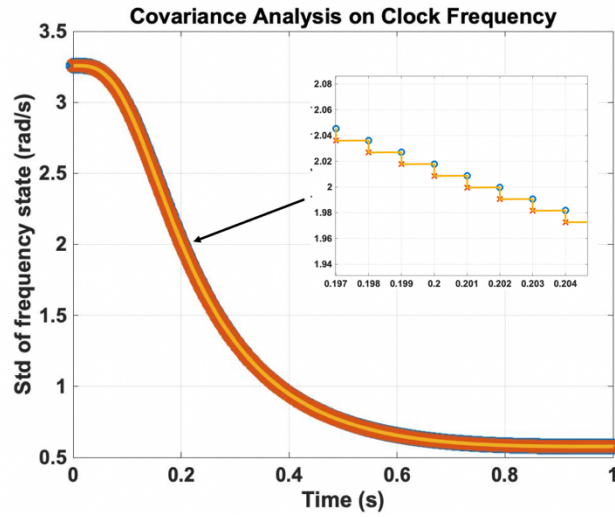


Fig. 9. Covariance analysis results

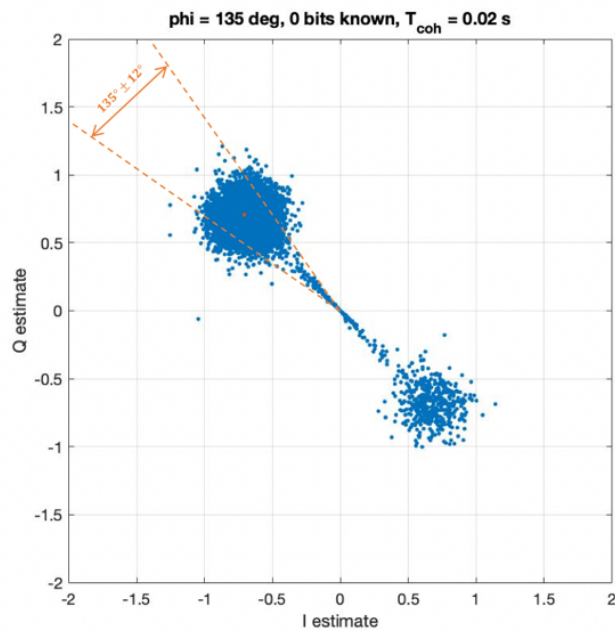


Fig. 10. IMM filter simulation

VI. EXPERIMENTAL SCENARIO AND SETUP

A. Experimental Scenario

In the interference scenario, the GPS receiver is operating under normal signal conditions prior to onset of the RFI event, so that the current ephemeris has already been decoded and will be valid for at least another two hours. The experiment covers a static GPS reference receiver over a 4-minute period with 5 satellites (PRN 1, 7, 11, 28, 30). The ephemeris file over that period is provided to the software-defined receiver (SDR). The onset of the RFI event is 2 minutes after start so that the receiver has

time to lock onto the nominal signals. The interference event is implemented by dropping C/N_0 from 51 dB/Hz (which was the nominal signal strength for all 4 satellites) as follows: no drop for PRN 1, 6 dB drop for PRN 30, 16 dB drop for PRN 7, 26 dB drop for PRN 11, and 36 dB drop for PRN 28.

B. Experimental Setup

GPS RF signals are generated using a Spectracom GSG- 6 GNSS simulator. A USRP N200 is used as the front end, and as noted earlier, two LPFRS Rubidium clocks are used as references for satellite and receiver. The IMM algorithm is implemented in a software defined receiver. Figure 11 shows the overview of the experimental setup.

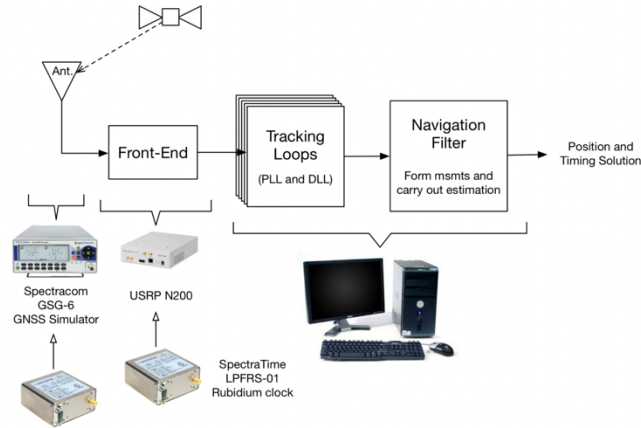


Fig. 11. Experimental setup

VII. IMM FILTER VALIDATION

When no interference is present, the IMM filter is expected to have essentially the same ‘tracking’ ability as a PLL. In this case, the PLL should provide a good reference for comparison. PRN 1 was free of interference over the entire 4-minute period, so it was used to test the IMM filter under nominal signal conditions. To do this we ran the PLL and IMM in parallel for PRN 1 and compared the reconstructed clock frequency output from both.

If the reconstructed clock frequency is the same from both, the total reconstructed carrier frequency will also be the same, because the remainder is due only to Doppler, which is also the same for both. As noted in Section VI-A the ephemeris file is available, so the Doppler feed into PLL and IMM is the same.

Figure 12 shows the details of the processing algorithm. The PLL maintains carrier frequency and phase lock at all times in this interference-free case, so the IMM can start at any time by taking the initial knowledge of the state vector from the PLL. After that, the IMM runs independently in parallel to the PLL. The measurement and dynamic model are provided in Sections II-B and II-A. The DLL needs the current carrier frequency to operate, which typically comes from the PLL. However, after we validate the IMM filter, we can draw the carrier frequency from the IMM. In this test, typical parameters are initially used in the PLL: third order loop filter and 1 ms coherent averaging time. The IMM filter starts at 80 sec.

The PLL noise bandwidth starts at 15 Hz, then to be optimized for the static receiver scenario gradually tightens to 1 Hz prior to start of IMM. Our observations of preliminary experimental results showed that when coherent averaging times are increased rapid tightening of PLL bandwidth after acquisition can cause the PLL to become unstable. Thus, a smooth polynomial function, Equation (10), was used to tighten the bandwidth B_n from 15 to 1 Hz in the first 70 sec, and then keep it at 1 Hz for the rest of the time.

$$B_n = 3e^{-19t^4} - 1.3e^{-13t^3} + 1.5e^{-8t^2} - 7e^{-4t} + 15.5 \quad (10)$$

where t is the elapsed time. It was not feasible to tighten the bandwidth to below 1 Hz because of PLL stability issues.

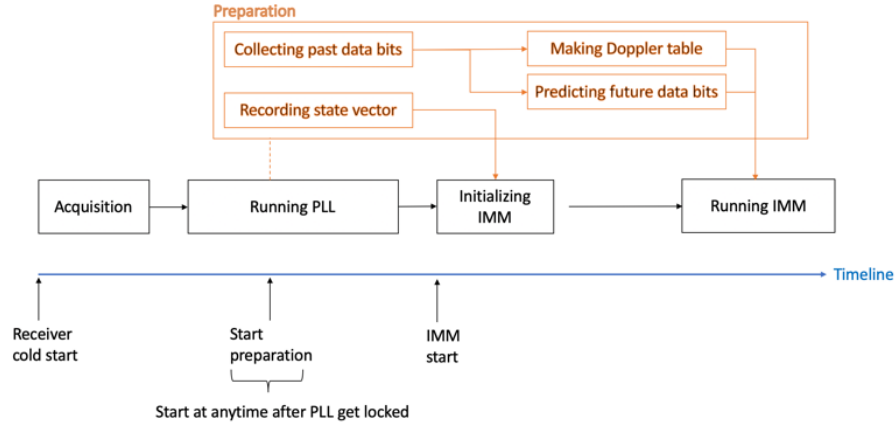


Fig. 12. IMM filter running logic

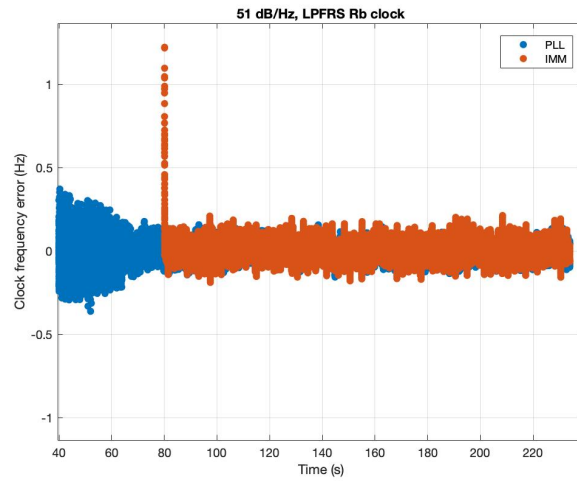


Fig. 13. Clock frequency error comparison (no interference)

Figure 13 shows the clock frequency error estimation results from the PLL and IMM. Blue lines stand for PLL and red lines stand for IMM, which starts at 80 seconds. After a short convergence transition period at 80 sec, the IMM filter clock frequency error estimation result matches the PLL result. The red and blue lines are nearly on top of each other which indicates that the IMM filter works as well as the PLL under the no interference case.

VIII. IMM FILTER PERFORMANCE IN INTERFERENCE

A. Interference Case: 15 dB/Hz

We perform the same test as in Section VII for PRN 28, which has a 36 dB/Hz drop in C/N_0 at 110 s. The PLL is still using a tightened bandwidth method from 15 Hz to 1 Hz in Equation (10) to handle the increased noise. As Figure 14 shows, although the PLL bandwidth has been tightened to 1 Hz, it is still not possible for the PLL to track the signal at 15 dB/Hz as the blue curve ramps up after encountering the interference event. This accumulated error will lead to cycle slips and eventually loss of lock. However, the IMM filter is still able to provide a reasonable clock frequency error estimation with zero mean and small drift as the red line shows. This result shows that the IMM filter is able to provide better carrier phase estimation even under an interference event with $C/N_0 = 15$ dB/Hz, while the PLL loses lock even when the noise bandwidth is tightened to the minimum value.

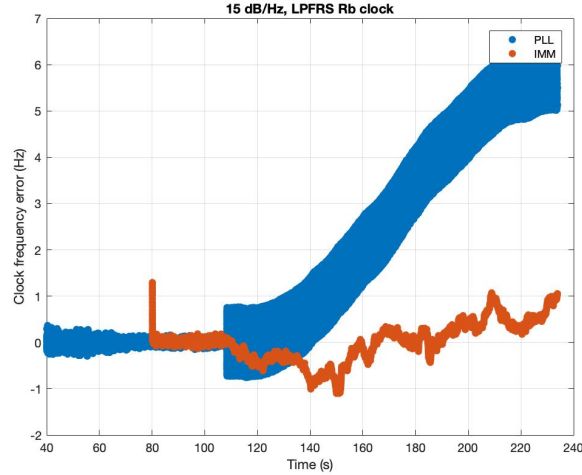


Fig. 14. Clock frequency error comparison (15 dB/Hz case)

IX. SENSITIVITY ANALYSIS FOR CLOCK MODEL

The motivation for using the Rubidium clock is that it allows the PLL to tighten to a narrower bandwidth to reject the noise. Since we have already shown that the IMM filter has the advantage over the PLL in both the normal and interference cases, we next determine whether the IMM filter can provide similar advantages with lower quality clocks. In simple terms, if the clock dynamic model is the crucial part that provides robustness for the IMM filter under an interference event, how much worse could we make the clock dynamic model to maintain IMM effectiveness?

To do the sensitivity analysis, we first need to set up a benchmark with which to compare. Here we are taking the clock frequency estimation result from PRN 1 (no interference) as the benchmark and consider five other cases:

- TCXO clock
- Manually inflating the Rubidium S_g parameter by 10^3 ; S_g is more related with low frequency clock errors
- Manually inflating the Rubidium S_f parameter by 10^3 ; S_f is more related with high frequency clock errors
- Manually inflating the Rubidium process noise matrix W by 10^3
- Manually inflating the Rubidium process noise matrix W by 10^7

We focus on the clock frequency error estimation and clock frequency error standard deviation. Figure 15 shows clock frequency error estimation results. Compared to the benchmark, inflating S_g by 10^3 does not seem to greatly impact the result which means our IMM filter is not sensitive to the S_g parameter. However, inflating S_f by 10^3 makes the variance on estimation much larger, so the TCXO clock model gets similar results because the S_f parameter of the TCXO is about 10^3 times that of the LPFRS Rubidium clock. These two results show that our IMM filter is sensitive to the S_f parameter. Inflating W by 10^3 inflates S_f and S_g at the same time. This gives the same result as inflating S_f only because S_g is not as important as the S_f parameter on the final result. Inflating W by 10^7 results in a huge variance simply because 10^7 is a big number.

Figure 16 shows clock frequency error standard deviation results. These six figures are the standard deviation of the results in Figure 15, respectively. We draw a similar conclusion in Figure 16 to that of Figure 15. If we inflate the S_f , the covariance will not converge and the IMM filter become unstable. In the last sub-figure of Figure 16, the covariance is so large that it exceeds the plot region and the plot appears blank.

From this sensitivity analysis, we see that the IMM filter result is sensitive to the S_f parameter corresponding to the high frequency part (short term stability) in the clock phase noise PSD plot. However, the Rubidium clock's advantage is mainly that it has better long-term stability. In future we would like to consider testing our IMM filter with OCXO clocks which are designed for better short-term stability.

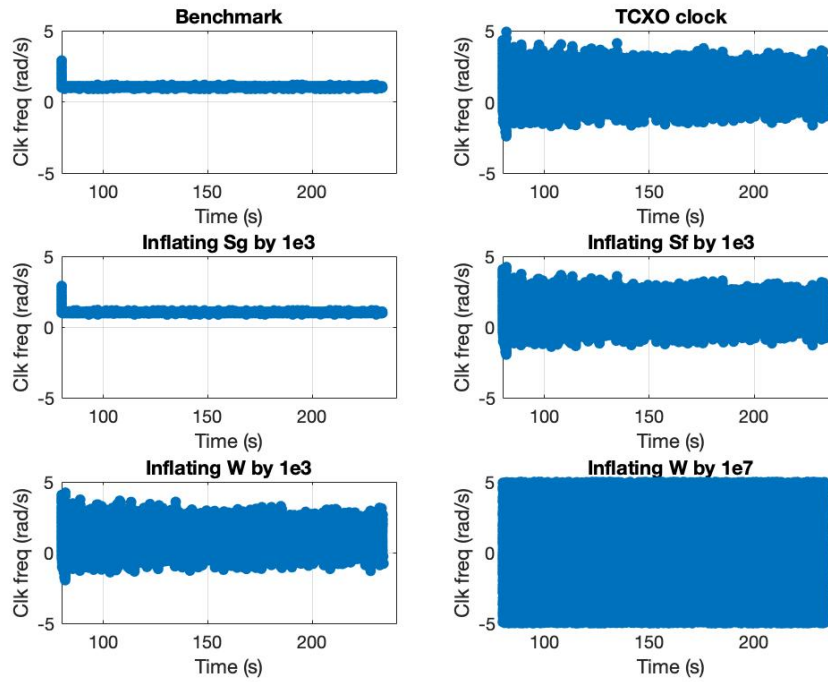


Fig. 15. Clock frequency error sensitivity analysis result

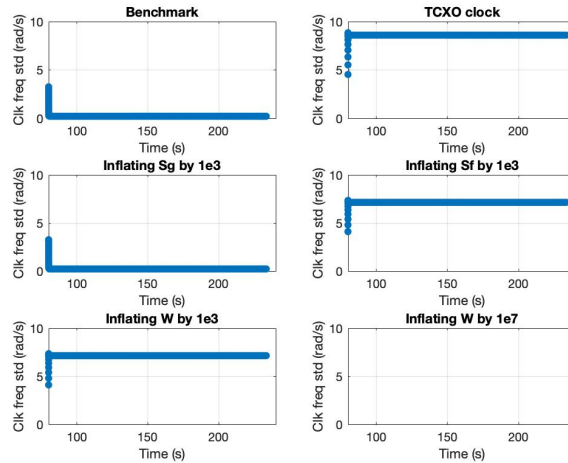


Fig. 16. Clock frequency error standard deviation sensitivity analysis result

X. CONCLUSION

In this paper, we bound the clock phase noise PSD and derive clock phase dynamic models under normal and vibration cases. Then we validate our IMM filter with this clock model with the experimental data. We prove that the performance of the IMM filter is better than traditional receiver PLL under both no interference and interference cases. A sensitivity analysis on clock dynamic model indicates that the IMM filter is more sensitive to the short term stability of the clock.

ACKNOWLEDGMENTS

We would like to thank our sponsors at the Federal Aviation Administration (FAA) for supporting this research. The views and opinions expressed in this paper are those of the authors and do not necessarily reflect those of any other organization or person.

REFERENCES

1. Pullen, S. and Gao, G. "GNSS Jamming in the Name of Privacy: Potential Threat to GPS Aviation," *Inside GNSS Magazine: Vol. 7 No. 2, March/April 2012*.
2. Zhao, W. and Pervan, B., "IMM Methods for Carrier Phase Tracking and Navigation Data Bits Estimation Through Interference," *Proceedings of the 2019 International Technical Meeting of The Institute of Navigation, Reston, Virginia, January 2019*, pp. 248-256.
3. Zhao, W. and Pervan, B., "Experimental Validation of IMM Algorithm for Carrier Phase Tracking Through Interference," *Proceedings of the 2020 International Technical Meeting of The Institute of Navigation, San Diego, California, January 2020*, pp. 315-319.
4. Zhao, W. and Pervan, B., "Data Bit Assisted Adaptive IMM Filter for Carrier Phase Tracking Through Interference," *Proceedings of the 33rd International Technical Meeting of the Satellite Division of The Institute of Navigation (ION GNSS+ 2020), September 2020*, pp. 3098-3107.
5. Bar-Shalom, Y., Li, X. R. and Kirubarajan, T., "Estimation with applications to tracking and navigation: theory algorithms and software," *John Wiley & Sons, 2004*.
6. "IEEE frequency and time standard," pp 27.
7. Chan, F., Joerger, M. and Pervan, B., "Stochastic modeling of atomic receiver clock for high integrity GPS navigation," *IEEE Transactions on Aerospace and Electronic Systems, vol. 50, no. 3, pp. 1749-1764, July 2014, doi:10.1109/TAES.2014.120402*.
8. Hegarty, C. J., "Analytical Derivation of Maximum Tolerable In-Band Interference Levels for Aviation Applications of GNSS," *NAVIGATION Journal of The Institute of Navigation, Vol. 44, No. 1, Spring 1997*, pp. 25-34.
9. "RTCA Environmental Conditions and Test Procedures for Airborne Equipment," *RTCA Document No. RTCA/DO-160C, December 1989*.